

Electron Paramagnetic Resonance Oxygen Mapping (EPROM): Direct Visualization of Oxygen Concentration in Tissue

S. Sendhil Velan,¹ Richard G.S. Spencer,¹ Jay L. Zweier,² and Periannan Kuppusamy^{2*}

Tissue oxygen content is a central parameter in physiology but is difficult to measure. We report a novel procedure for spatial mapping of oxygen by electron paramagnetic resonance (EPR) utilizing a spectral-spatial imaging data set, in which an EPR spectrum is obtained from each image volume element. From this data set, spatial maps corresponding to local spin density and maximum EPR spectral line amplitude are generated. A map of local EPR spectral linewidth is then computed. Because linewidth directly correlates with oxygen concentration, the linewidth image provides a map of oxygenation. This method avoids a difficulty inherent in other oxygen content mapping techniques using EPR, that is, the unwanted influence of local spin probe density on the image. We provide simulation results and data from phantom studies demonstrating the validity of this method. We then apply the method to map oxygen content in rat tail tissue and vasculature. This method provides a new, widely applicable, approach to direct visualization of oxygen concentration in living tissue. Magn Reson Med 43: 804–809, 2000. © 2000 Wiley-Liss, Inc.

Key words: EPR; EPR imaging; oximetry; nitroxide

The vast majority of energy generation in living systems is provided by aerobic metabolism. This mechanism requires an adequate supply of oxygen to act as the final electron acceptor of the mitochondrial electron transport chain. Pathology related to lack of oxygen, and hence inadequate energy supply, is widespread, and includes entities such as coronary artery and peripheral vascular disease and stroke. Further, oxygen is known to be a promoter of pathology related to excessive free radical generation (1), as seen for example in reperfusion injury in muscle or brain. Accordingly, there has been a great deal of interest in developing methods for measuring tissue oxygen content in living systems (2–7).

Electron paramagnetic resonance (EPR) spectroscopy and imaging techniques have been used extensively to probe parameters of physiologic importance, such as tissue metabolic activity, redox state, and oxygen (7–9). These techniques require the incorporation of a suitable paramagnetic spin label into the system under investigation. The principle of oximetry by EPR is based on the paramagnetic characteristics of molecular oxygen, which in its ground state has two unpaired electrons, and under-

goes Heisenberg spin exchange interaction with the paramagnetic EPR spin probe. This process is sensitive to oxygen content, with the relaxation rate of the spin probe increasing as a function of oxygen content. This increased spin-spin relaxation rate results in increased line broadening. According to Smoluchowsky theory, the oxygen-broadened linewidth is directly proportional to oxygen concentration. The fact that the linewidths of EPR resonance lines correlate with oxygen concentration has been used in a variety of biological settings (6,7,9–11). In each case, accurate measurement of oxygen-induced line broadening requires the presence of a suitable EPR probe. In general, particulate probes such as lithium phthalocyanine (10,12) and synthetic char (13) are suitable for measurements of oxygen partial pressure, whereas soluble probes such as nitroxides and trityl compounds (14–16) measure dissolved oxygen concentration.

Besides spectroscopic studies, EPR has also been developed as an *in vivo* imaging method (17) to map the distribution of an incorporated spin label. One of the major focuses of EPR imaging has been to map the spatial distribution of dissolved oxygen in tissue (7). Methods have been developed to produce image contrast based on oxygen-induced line broadening. Subtraction techniques involve acquiring images with and without oxygen perfusion (18). Oxygen maps may also be obtained with variable microwave power levels, since saturation depends on oxygen concentration. Another approach has been to look at the oxygen-dependent metabolism of nitroxides to indicate differences in oxygen concentration (18). In these studies, maps of oxygen must be interpreted in light of possible variations in nitroxide concentration, rendering the data difficult to interpret.

EPR spectral-spatial (or spectroscopic) imaging is a technique providing an EPR spectrum for each voxel in an image data set (19). This method has been successfully applied to a number of biological systems (7,20,21). Because the spatial and spectral dimensions are fully separable, information about local linewidth, and hence local oxygen content, can in principle be derived independently from local spin density. Accordingly, we describe here a new technique, which we call EPR oxygen mapping (EPROM), for producing spatial maps of linewidth using a spectral-spatial EPR data set. This linewidth map is then translated to an oxygen map by appropriate calibration.

THEORY

The relationships among line amplitude, linewidth, and area are well defined for the commonly encountered EPR absorption lineshapes, that is, Lorentzian and Gaussian. In

¹Nuclear Magnetic Resonance Unit, National Institute on Aging, National Institutes of Health, Baltimore, Maryland.

²The EPR Center, Division of Cardiology, Department of Medicine, Johns Hopkins University, School of Medicine, Baltimore, Maryland.

Grant sponsor: National Cancer Institute; Grant number: CA-78886-01; Grant sponsor: National Institutes of Health; Grant number: RR-12190.

*Correspondence to: Periannan Kuppusamy, EPR Center, Johns Hopkins University, School of Medicine, 5501 Hopkins Bayview Circle, Baltimore, MD 21224. E-mail: kupp@welch.jhu.edu

Received 28 July 1999; revised 28 January 2000; accepted 31 January 2000.

these cases, the area is proportional to the product of the peak amplitude and the linewidth, measured, for example, by the full width at half maximum (FWHM). The Voigt lineshape, a convolution of Lorentzian and Gaussian lineshapes, can be treated by deconvolution techniques (22,23).

The area of a Lorentzian absorption line, A_L , is given by (22):

$$A_L = (\pi/2) Y_L^{\max} \Gamma \quad [1]$$

where Y_L^{\max} is the amplitude maximum, and Γ is the FWHM. The corresponding expression for gaussian absorption lines is (22)

$$A_G = 1.065 Y_G^{\max} \Gamma. \quad [2]$$

In general, in EPR spatial imaging, an array is constructed that corresponds to the spectral line amplitude at the resonant field, that is, at $B = B_0$. Therefore, for a given linewidth, greater local spin density results in greater image intensity, whereas for a given local spin density, greater linewidth results in a smaller value for the maximum spectral line amplitude, that is, lower image intensity. Thus, the spatial array corresponding to $B = B_0$ reflects both spin density and linewidth at each spatial location. In contrast, a true spectral-spatial image data set provides the complete absorption profile for the spectrum corresponding to each voxel in the sample. Therefore, integration can be performed over the spectral, or field, dimension to obtain the spin density within the voxel. Thus, spectral-spatial imaging can provide a spatial map of spin density, independent of local linewidth.

The local linewidth can be computed directly from the spatial maps of spin density and maximum spectral line amplitude. Assuming that (i) the measurements are performed under low-modulation and nonsaturating experimental conditions, so the measured spin density of a paramagnetic probe is directly related to the area under the EPR absorption spectrum, (ii) the lineshape of the absorption profile from spins of each voxel may be expressed by a Lorentzian or Gaussian lineshape, and (iii) the lineshape function is invariant over the entire set of voxels, then the linewidth at a given voxel (Γ_v) is given by:

$$\Gamma_v = \kappa A/Y^{\max} \quad [3]$$

where κ is a constant for a given lineshape and A denotes the area of the spectral line. This computation may be performed over the entire image array to produce a spatial map of linewidth. It should, however, be noted that the constant κ might take on different values depending on the lineshape. As the EPR lineshape is modeled as a convolution of a Lorentzian shape (due to oxygen broadening) and Gaussian shape (due to unresolved hyperfine splitting and other random processes), the lineshape will be increasingly Lorentzian in shape at higher oxygen broadening. Thus, the value of κ may vary from 1.065 for pure gaussian to $\pi/2$ for pure Lorentzian. This constant can be calculated by detailed lineshape analysis. A specific lineshape can be assumed for linewidth estimations.

Equation [3] must be modified to account for realistic imaging conditions. Signals from voxels within the imaging field of view but which are beyond the boundaries of the object produce only noise, resulting in local values for Γ_v that have no physical meaning. Similar comments apply to signal from regions within the sample but with very low image intensity, due either to large local linewidth or to low spin probe concentration. Therefore, it is useful to set $\Gamma_v = 0$ for all regions for which the signal amplitude falls below a fixed cutoff. In addition, upper and lower limits to Γ_v can be set based on the linewidths corresponding to the expected range of oxygen concentrations as determined by calibration experiments for the oximetry probe employed.

MATERIALS AND METHODS

Phantom Construction

A phantom was constructed with six identical tubes (inner diameter, 4.1 mm) filled with different concentrations of ^{15}N -labeled 4-oxo-2,2,5,5-tetramethylpyrrolinyl- d_{16} - N -oxy (perdeuterated tempone, PDT) and chromium oxalate (CrOx), diluted in Dulbecco's phosphate-buffered saline. The tubes were filled to a height of 4 cm, with the solution extending vertically both above and below the active region of the microwave cavity.

Calibration

Calibration of oxygen-induced line broadening as a function of oxygen partial pressure was performed on a saline solution of 0.25 mM PDT by equilibrating with mixtures of nitrogen and oxygen gases. Observed peak-to-peak widths varied almost linearly from 0.28 G for 0% oxygen to 1.05 G for 100% oxygen, thus, a total range of 0.77 G line-broadening is available (Fig. 1). Because precise maintenance and equilibration of different oxygen/nitrogen gas mixtures in a small volume of multiple tubes is difficult, we chose to use potassium CrOx, a paramagnetic broadening agent, to cause equivalent line broadening. A calibration curve for the line broadening of PDT as a function of CrOx concentration is shown in Fig. 1. It is observed that both oxygen and CrOx produced almost identical linewidth variation, approximated by a linear variation of 7.7 ± 0.4 mG/% oxygen or 150 ± 8 mG/mM CrOx. Thus, 1 mM CrOx was equivalent to 20% oxygen in causing line-broadening (T_2) of 0.25 mM PDT solution under identical spectral/image acquisition settings. Because the aim of this work was to demonstrate the ability of obtaining linewidth maps using EPR imaging, the source of line broadening is immaterial. Hence in some of the phantom experiments, we used CrOx to produce line-broadening variations.

Animal Preparation

Female Sprague-Dawley retired breeder rats weighing 325 ± 25 g were used. The rats were anesthetized with a combination of ketamine (80 mg kg^{-1}) and xylazine (5 mg kg^{-1}) injected intraperitoneally. A bolus dose of 185 mg/kg of 3-carbamoyl-2,2,5,5-tetramethyl-pyrrolidine- N -oxyl (3-CP) in 1.0 ml saline was infused via tail vein cannulation.

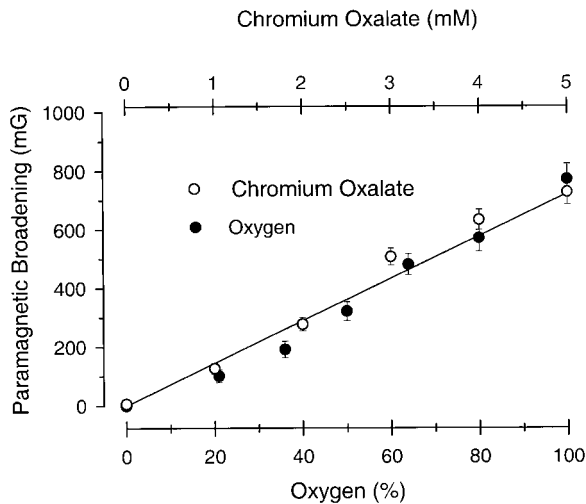


FIG. 1. Calibration of EPR line-broadening as a function of oxygen partial pressure and chromium oxalate (CrOx). The oxygen calibration experiments were performed at 25°C, on a saline solution of 0.25 mM PDT by equilibrating with mixtures of nitrogen and oxygen gases. Observed broadening peak-to-peak widths varied almost linearly from 0 MG for 0% oxygen to 770 MG for 100% oxygen. Also shown is a calibration curve for the line broadening of PDT as a function of CrOx concentration. The data points shown are mean values of at least three measurements. It was observed that both oxygen and CrOx produced almost identical variation, approximated by a linear variation of 7.7 ± 0.4 mG/% oxygen or 150 ± 8 mG/mM CrOx.

The tail was positioned in the bore of a reentrant resonator. The rat breathed ambient air ($\sim 21\%$ oxygen).

EPR Equipment

The imaging experiments were performed using the L-band EPR imaging system reported previously (24). A ce-

ramic 3-loop 2-gap reentrant resonator with a central bore of 20 mm diameter was used for all the experiments (25). The resonant frequency was 1.21 GHz.

EPR Methodology

Optimal selection of data acquisition parameters and object centering within the cavity were performed by acquiring 2D spatial images of the object. Three-dimensional spectral-spatial projection data were acquired using angularly sampled gradient fields. Field modulation was kept at less than one-third of the minimum linewidth to avoid over-modulation. Projection data acquisition and subsequent image reconstruction were performed using a personal computer with custom software. For phantom experiments involving PDT, a total of 576 (24×24) projections were acquired over a field of view (FOV) of 4.0 G in the spectral dimension and 20 mm \times 20 mm in the cross-sectional spatial dimensions. The images were corrected for hyperfine artifacts (26), and reconstructed using filtered back-projection methods.

RESULTS

Figure 2 shows images of a six-tube phantom containing saline solutions of PDT with concentration ranging from 0.25 to 0.50 mM. CrOx was added to each tube to induce T_2 broadening equivalent to oxygen contents ranging from 21-96%. Spatial maps are displayed that correspond to (a) maximum amplitude at resonance field, (b) total spin density, and (c) oxygen-induced broadening. The spatial map, which gives the maximum amplitude of the signal at each voxel, reflects the combination of spin density and linewidth, as discussed above. Neither the spin density nor the linewidth information can be directly visualized from this image. On the other hand, the intensity map, which was

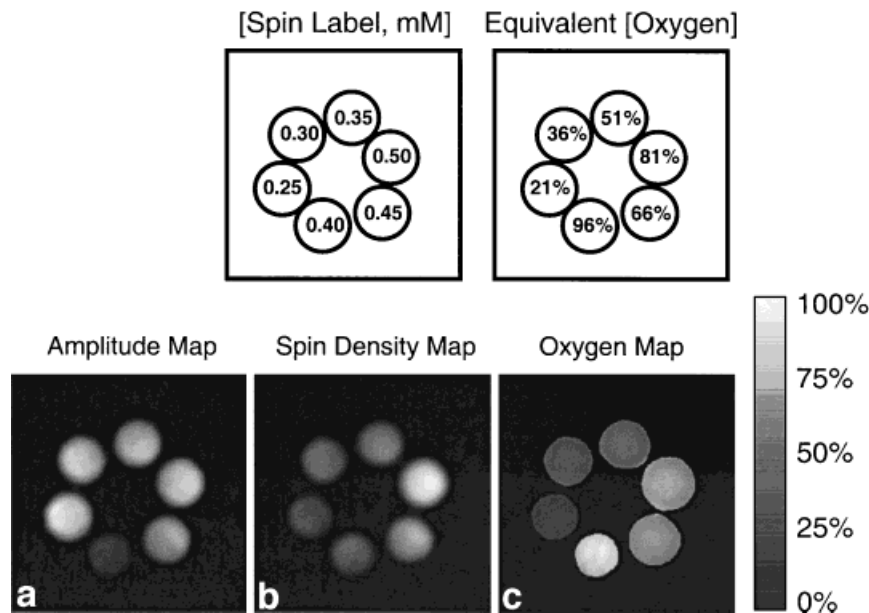


FIG. 2. Demonstration of the EPROM method on a six-tube phantom. Phantom construction is described in the text. The top panels show the spatial arrangement and characteristics of the phantom. **a**: Spatial map corresponding to maximum amplitude. **b**: Spatial distribution of spin density. **c**: Oxygen map. The gray-scale at right shows the equivalent oxygen concentration based on linewidth. The oxygen concentrations seen in **c** are in good agreement with the phantom characteristics.

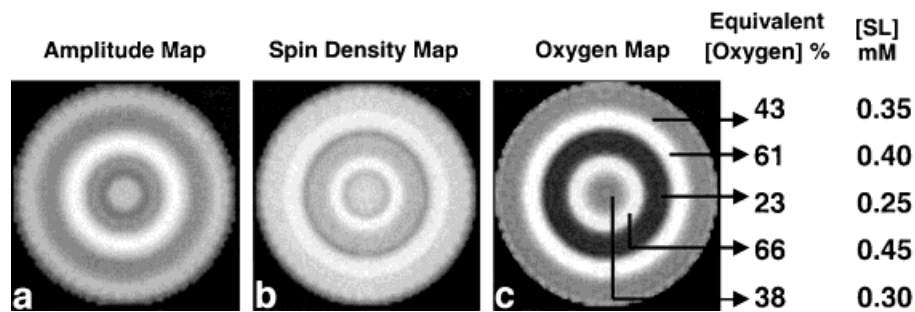


FIG. 3. Demonstration of the EPROM method on a simulated phantom. The phantom consisted of five concentric tubes containing different concentrations of spin label (SL) and oxygen, as specified. The results of oxygen mapping using the data displayed in panels **a** and **b**, as shown in panel **c**, are consistent with the simulation and input parameters.

obtained by converting the 3D spectral-spatial data set to a 2D spatial image by integration over the spectral dimension, provides direct visualization of spin density within the phantom. Accordingly, the intensity map is independent of linewidth and amplitude, and corresponds well with the concentrations of PDT in the phantom tubes as shown in the top-left panel. Similarly, the linewidth map corresponds purely to equivalent oxygen content as shown in the top-right panel.

Figure 3 displays simulated EPR images of a hypothetical oximetry phantom consisting of five concentric tubes. Each tube was assigned the indicated oximetry probe concentration and oxygen partial pressure. The linewidths ranged from 0.35 G to 0.80 G corresponding to 38%–66% oxygen, using a hypothetical oximetry probe exhibiting 0.25 G anoxic linewidth. The images were reconstructed from 576 (24×24) simulated projections with a 3D FOV of 4.00 G in the spectral dimension and 20 mm \times 20 mm in the spatial dimensions. The amplitude and spin density images show image contrast produced as described above for the phantom. The linewidth map computed from these images and converted to equivalent oxygen concentration is seen to be invariant to spin label concentration differences, but rather reflects linewidth only, as desired.

To further demonstrate the applicability of this method, we imaged the cross-sectional anatomy and oxygenation of the rat tail infused with a nitroxide label. We used 3-CP as it is more stable in tissues than PDT, though 3-CP is less

sensitive to oxygen due to its large peak-to-peak linewidth, 1.22 G at 0% oxygen (9). As described in the Methods section, rats were infused with 3-CP label and breathed ambient air ($\sim 21\%$ oxygen). A total of 256 projections were collected using a spectral window 6.5 G and modulation amplitude 0.3 G. Figure 4 shows cross-sectional spatial maps obtained from a typical experiment: (a) maximum amplitude in the spectral dimension, (b) local spin label density, and (c) oxygen distribution. The contrast observed in the oxygen map clearly shows the difference in tissue oxygen perfusion. It has been reported (27,28) that rat tail consists of three different layers: bone, tendon, and cutaneous. The artery and veins of the tail exist as pairs, which are embedded in the tendon at the interface with the cutaneous layer. At least three major artery-vein pairs have been identified, while there are a number of other smaller radial supply vessels (27). The cross-sectional spin density images of the tail show four prominent regions of nitroxide concentration. These regions appear to correspond to the major vessels and surrounding tissue and muscle bundles, which are separated by bone (27). Anatomical distinction between the artery and vein is not possible based on the distribution of the nitroxide, which distributes into extravascular regions. However, the oxygen map (c) clearly shows the existence of oxygen gradients from the center of the four regions where major vessels are located to distal regions. The observed drop in oxygen concentration away from the

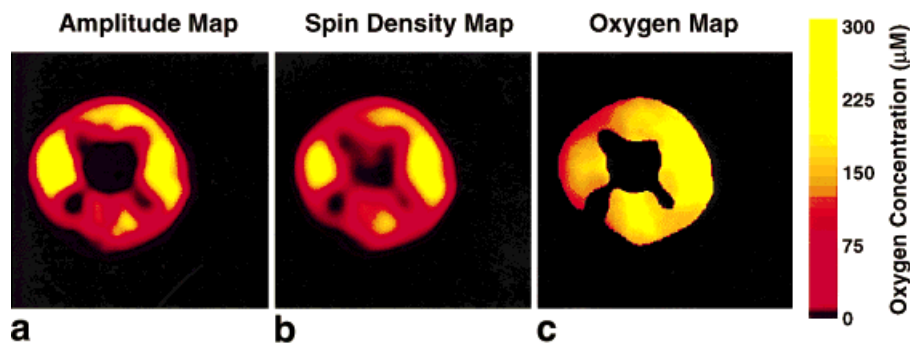


FIG. 4. Application of the EPROM method to a rat tail, in vivo. The rat was loaded (i.v.) with 185 mg/kg of 3-CP with its tail positioned in the bore of a reentrant resonator as described in the Methods section. Data acquisition was started 25 min after the label was infused. 3D spectral-spatial images were reconstructed from 256 projections. In vivo maps of (a) maximum spectral line amplitude, (b) spin label density, and (c) oxygenation in the rat-tail cross-section are shown.

center of the regions may be due to oxygen consumption by the surrounding muscle tissue. Based on our calibrations, a maximum oxygen concentration of $300 \pm 30 \mu\text{M}$ was obtained at the center of these regions by the EPROM method. The maximum value and its error limit were obtained from a small area comprising of 5 voxels centered in the region of interest.

DISCUSSION

There are a number of modalities available for in vivo oxygen measurements. Methods that utilize microelectrodes, while having very high spatial and temporal resolution, are highly invasive and require extensive sample preparation (4). Protocols have also been developed employing ^{19}F MRS and MRI, based on the effect of oxygen to alter nuclear relaxation rates (29–31). In addition, the degree of myocellular oxygenation has been assessed by measurements of myoglobin signals in muscle and heart using proton NMR spectroscopy (32). Further, functional brain imaging in MRI is based on oxygen-induced changes of magnetic susceptibility (33). EPR imaging protocols add importantly to the NMR methods described above. They are minimally invasive, and a wide variety of spin probes are available for specific purposes. However, several factors, including limited spatial resolution and signal-to-noise ratio restrict the accuracy with which the oxygen distribution can be measured. Spectral fitting procedures (7,23) have been employed for smoothing and extracting linewidth and oxygenation parameters from the spectral-spatial image data. However, none of the above methods directly yield spatial maps of oxygen content.

Here, we have described a new technique for directly producing a spatial map of oxygen in vivo in which local image intensity is a function of linewidth alone. We have demonstrated the validity of this technique using phantoms, computer simulations, and an in vivo arteriovenous measurement of oxygenation in the tail of a living rat. Unlike the spectral-fitting method of Halpern (7,23), EPROM does not require parameterization of oxygen-induced changes in lineshapes. Our method is applicable to systems that have, in general, simple lineshapes that can be approximated by Gaussian or Lorentzian shapes, whose area under the absorption curve is directly related to its amplitude and width. Such lineshapes are commonly encountered in nitroxide-based EPR oximetry experiments.

The accuracy of the EPROM method, however, depends on several factors. The most important factor is the accuracy with which double integration can be performed on the spectral data. Because EPR imaging necessitates the use of small sweep-widths, double integration of Lorentzian shapes in particular will introduce truncation artifacts. Though the use of 6.5 G sweep for a probe of 1.2 G anoxic linewidth may not be the optimum value for integration alone, its use is justified based on other limitations to resolution. On the other hand, one may use spectral fitting procedures to compute the area of the absorption curve for each voxel, and then use EPROM to compute the linewidth map. The accuracy of the method is also compromised, though to a lesser extent, by the effect of viscosity differences in tissue fluids. Because viscosity effects broaden nitroxide spectral lines, the EPR-based oximetry

techniques tend to over-estimate the tissue oxygen content.

Another important factor that may affect the accuracy of measuring oxygen concentration in biological tissue with any EPR oximetry method is the existence of substantially different oxygen solubilities in lipid-rich and aqueous compartments within the tissue. The oxygen concentration in water equilibrated with room-air, corresponding to a partial pressure of oxygen ~ 160 mmHg, at 37°C , is approximately $224 \mu\text{M}$. However, the oxygen solubility in lipids may be enhanced by a factor of up to 5 compared to that in the aqueous phase. It should be noted that the measured oxygen concentration of $300 \mu\text{M}$ is twice of that expected from an aqueous sample at arterial saturation (~ 100 mmHg). Nitroxide probes, such as the 3-CP, that distribute both in the aqueous compartment and the lipid compartment might report a higher oxygen concentration than expected from a pure aqueous phase, at any given oxygen partial pressure. Further, in our spectral-spatial imaging the spectral information was obtained from a 2-D projection of the tail, wherein the spatial information along the long axis of the tail was not resolved. This might contribute to the difficulty in the precise location of the artery. Thus the measured value of oxygen at the arterial location should be treated as an estimate from a circular area (of 3 pixels or ~ 1 mm diameter) centered about the artery that will include some overlap with the muscle bundles outside the vessel. Thus, the measured oxygen concentration in the arterial locations cannot be interpreted as a true quantitative measure from the aqueous phase of the artery alone.

It should be noted that these problems are common to EPR-based oximetry methods. Nevertheless, the proposed algorithm for computing oxygen-induced linewidth maps in intact biological samples should provide useful semi-quantitative measurements of voxel oxygen concentrations. With careful consideration of the factors discussed above a fully quantitative mapping of oxygen should be possible in a wide variety of in vitro and in vivo systems.

ACKNOWLEDGMENTS

We thank Dr. K.W. Fishbein and Dr. G. Ilangovan for their technical help. P.K. was supported by an Established Investigator Award from the American Heart Association during the tenure of this study.

REFERENCES

1. Moslen MT, Smith CV. Free radical mechanisms of tissue injury. Boca Raton, FL: CRC Press, Inc.; 1992.
2. Lubbers DW, Huch R, Huch A. Problems of transcutaneous measurement of arterial blood gases. *Adv Exp Med Biol* 1973;37A:115–120.
3. Keizer HH, Jobsis-Vander Vleit FF, Lucas SS, Piantadosi CA, Sylvia AL. The near infrared (NIR) absorption band of cytochrome aa3 in purified enzyme, isolated mitochondria and in the intact brain in situ. *Adv Exp Med Biol* 1985;191:823–832.
4. Linsenmeier RA, Yancey CM. Improved fabrication of double-barreled recessed cathode O_2 microelectrodes. *J Appl Physiol* 1987;63:2554–2557.
5. Fishman JE, Joseph PM, Carvlin MJ, Saadi-elmandjra M, Mukherji B, Sloviter HA. In vivo measurements of vascular oxygen tension in tumors using MRI of a fluorinated blood substitute. *Invest Radiol* 1989; 24:65–71.

6. Swartz HM, Boyer S, Brown D, Chang K, Gast P, Glockner JF, Hu H, Liu KJ, Moussavi M, Nilges M, Norby SW, Smirnov A, Vahidi T, Walczak T, Wu M, Clarkson RB. The use of EPR for the measurement of the concentration of oxygen in vivo in tissues under physiologically pertinent conditions and concentrations. *Adv Exp Med Biol* 1992;317:221–228.
7. Halpern HJ, Yu C, Peric M, Barth E, Grdina DJ, Teicher BA. Oxymetry deep in tissues with low-frequency electron paramagnetic resonance. *Proc Natl Acad Sci USA* 1994;91:13047–13051.
8. Kuppusamy P, Afeworki M, Shankar RA, Coffin D, Krishna MC, Hahn SM, Mitchell JB, Zweier JL. In vivo electron paramagnetic resonance imaging of tumor heterogeneity and oxygenation in a murine model. *Cancer Res* 1998;58:1562–1568.
9. Kuppusamy P, Shankar RA, Zweier JL. In vivo measurement of arterial and venous oxygenation in the rat using 3D spectral-spatial electron paramagnetic resonance imaging. *Phys Med Biol* 1998;43:1837–1844.
10. Liu KJ, Gast P, Moussavi M, Norby SW, Vahidi N, Walczak T, Wu M, Swartz HM. Lithium phthalocyanine: a probe for electron paramagnetic resonance oximetry in viable biological systems. *Proc Natl Acad Sci USA* 1993;90:5438–5442.
11. Liu KJ, Bacic G, Hoopes PJ, Jiang J, Du H, Ou LC, Dunn JF, Swartz HM. Assessment of cerebral pO₂ by EPR oximetry in rodents: effects of anesthesia, ischemia, and breathing gas. *Brain Res* 1995;685:91–98.
12. Glockner JF, Swartz HM. In vivo oximetry using two novel probes: fusinite and lithium phthalocyanine. *Adv Exp Med Biol* 1992;317:229–234.
13. Zweier JL, Chzhan M, Ewert U, Schneider G, Kuppusamy P. Development of a highly sensitive probe for measuring oxygen in biological tissues. *J Magn Reson B* 1994;105:52–57.
14. Glockner JF, Norby SW, Swartz HM. Simultaneous measurement of intracellular and extracellular oxygen concentrations using a nitroxide-liposome system. *Magn Reson Med* 1993;29:12–18.
15. Kuppusamy P, Wang P, Chzhan M, Zweier JL. High resolution electron paramagnetic resonance imaging of biological samples with a single line paramagnetic label. *Magn Reson Med* 1997;37:479–483.
16. Murugesan R, Cook JA, Devasahayam N, Afeworki M, Subramanian S, Tschudin R, Larsen JA, Mitchell JB, Russo A, Krishna MC. In vivo imaging of a stable paramagnetic probe by pulsed-radiofrequency electron paramagnetic resonance spectroscopy. *Magn Reson Med* 1997;38:409–414.
17. Eaton GR, Eaton SS, Ohno K. EPR imaging and in vivo EPR. Boca Raton, FL: CRC Press, Inc.; 1991.
18. Swartz HM, Glockner JF. Measurement of oxygen by EPRI and EPRS. In: Eaton GR, Eaton SS, Ohno K, editors. *EPR imaging and in vivo EPR*. Boca Raton, FL: CRC Press, Inc.; 1991. p 261–290.
19. Maltempo MM, Eaton SS, Eaton GR. Spectral-spatial two-dimensional EPR imaging. *J Magn Reson* 1987;72:449–455.
20. Kuppusamy P, Chzhan M, Vij K, Shteynbuk M, Lefer DJ, Giannella E, Zweier JL. Three-dimensional spectral-spatial EPR imaging of free radicals in the heart: a technique for imaging tissue metabolism and oxygenation. *Proc Natl Acad Sci USA* 1994;91:3388–3392.
21. Kuppusamy P, Chzhan M, Samouilov A, Wang P, Zweier JL. Mapping the spin-density and lineshape distribution of free radicals using 4D spectral-spatial EPR imaging. *J Magn Reson B* 1995;107:116–125.
22. Poole CP. *Electron spin resonance, a comprehensive treatise on experimental techniques*. New York: John Wiley & Sons; 1983.
23. Halpern HJ, Peric M, Yu C, Bales BL. Rapid quantitation of parameters from inhomogeneously broadened EPR spectra. *J Magn Reson A* 1993;103:13–22.
24. Zweier JL, Kuppusamy P. Electron paramagnetic resonance measurements of free radicals in the intact beating heart: a technique for detection and characterization of free radicals in whole biological tissues. *Proc Natl Acad Sci USA* 1988;85:5703–5707.
25. Chzhan M, Kuppusamy P, Zweier JL. Development of an electronically tunable L-band resonator for EPR spectroscopy and imaging of biological samples. *J Magn Reson B* 1995;108:67–72.
26. Kuppusamy P, Zweier JL. A forward-subtraction procedure for removing hyperfine artifacts in electron paramagnetic resonance imaging. *Magn Reson Med* 1996;35:316–322.
27. Wu Y, Jiji LM, Lemons DE, Weinbaum S. A non-uniform three-dimensional perfusion model of rat tail heat transfer. *Phys Med Biol* 1995;40:789–806.
28. Tsoref L, Shinar H, Seo Y, Eliav U, Navon G. Proton double-quantum filtered MRI—a new method for imaging ordered tissues. *Magn Reson Med* 1998;40:720–726.
29. Mason RP, Shukla H, Antich PP. In vivo oxygen tension and temperature: simultaneous determination using ¹⁹F NMR spectroscopy of perfluorocarbon. *Magn Reson Med* 1993;29:296–302.
30. Parhami P, Fung BM. Fluorine-19 relaxation study of perfluoro chemicals as oxygen carriers. *J Phys Chem* 1983;87:1928–1931.
31. Taylor J, Deutsch C. ¹⁹F—Nuclear magnetic resonance: measurements of O₂ and pH in biological systems. *Biophys J* 1988;53:227–233.
32. Mancini DM, Wilson JR, Bolinger L, Li H, Kendrick K, Chance B, Leigh JS. In vivo magnetic resonance spectroscopy measurement of deoxy-myoglobin during exercise in patients with heart failure. *Circulation* 1994;90:500–508.
33. Zhu XH, Kim SG, Andersen P, Ogawa S, Ugurbil K, Chen W. Simultaneous oxygenation and perfusion imaging study of functional activity in primary visual cortex at different visual stimulation frequency: quantitative correlation between BOLD and CBF changes. *Magn Reson Med* 1998;40:703–711.